Engineering geometrical 3-dimensional untethered in vitro neural tissue mimic

Gelson J. Pagan-Diaz[a], Karla P. Ramos-Cruz[a], Richard Sam[b], Mikhail E. Kandel[c], Onur Aydin[d], M. Taher A. Saif[d], Gabriel Popescu[a,c], and Rashid Bashir[a,1]

[a]Department of Bioengineering, University of Illinois, Urbana–Champaign, Urbana, IL 61801; [b]School of Molecular and Cellular Biology, University of Illinois, Urbana–Champaign, Urbana, IL 61801; [c]Department of Electrical and Computer Engineering, University of Illinois, Urbana–Champaign, Urbana, IL 61801; and [d]Department of Mechanical Science and Engineering, University of Illinois, Urbana–Champaign, Urbana, IL 61801

Formation of tissue models in 3 dimensions is more effective in recapitulating structure and function compared to their 2-dimensional (2D) counterparts. Formation of 3D engineered tissue to control shape and size can have important implications in biomedical research and in engineering applications such as biological soft robotics. While neural spheroids routinely are created during differentiation processes, further geometric control of in vitro neural models has not been demonstrated. Here, we present an approach to form functional in vitro neural tissue mimic (NTM) of different shapes using stem cells, a fibrin matrix, and 3D printed molds. We used murine-derived embryonic stem cells for optimizing cell-seeding protocols, characterization of the resulting internal structure of the construct, and remodeling of the extracellular matrix, as well as validation of electrophysiological activity. Then, we used these findings to biofabricate these constructs using neurons derived from human embryonic stem cells. This method can provide a large degree of design flexibility for development of in vitro functional neural tissue models of varying forms for therapeutic biomedical research, drug discovery, and disease modeling, and engineering applications.

neural construct | biofabrication | tissue mimic | mESC | hESC

The design of living tissue to create specific shapes and forms is arguably one of the main obstacles in the forward design of engineered tissues, cellular systems, and biological machines. Given the fact that 3-dimensional (3D) structures are critical to recapitulate many physiologically relevant characteristics, a major goal of tissue engineering is to achieve customizable and viable 3D cell cultures. To an extent, this has been achieved by engrafting cells of interest on synthetic structures (1), or more recently providing cells with protein matrices such as Matrigel and fibrin, which facilitate cell–cell and cell–extracellular matrix (ECM) interactions (2–5). This approach creates a liquid state of protein-rich solutions mixed with cells. After subsequent polymerization, 3D structures are formed and the cells are allowed to grow and function (Fig. 1A).

Such an approach has been used to differentiate progenitor cells toward developing functional organoids that mimic physiological morphologies and functions. For example, muscle cells have been differentiated into actuating tissue for development of biohybrid actuators for soft robotics (6, 7), to develop models for drug discovery or therapeutic studies (2, 8), as well as for studies on healing in 3D and tissue regeneration (9, 10). An interesting observation has been that, by providing a mold during the culture, the cell–matrix solution can be compacted into stable geometries due to internal stresses generated by traction forces generated by the engrafted cells (11). In other words, the shape of the resulting construct can be determined by the 3D printed molds, which are fabricated using bioprinting approaches, such as a stereolithography apparatus (SLA) 3D printer (Fig. 1B). Given the needs and interests in 3D neuroengineering, using this approach of cell–matrix compaction for the formation of controlled 3D neural architectures could be highly beneficial.

Currently, 3D neural tissue is often obtained from animal models or from spherical embryoid bodies (EBs) spontaneously formed during stem cell differentiation (12–14). These EBs are currently unable to be scaled up due to diffusion limitations, placing limitations on their compatibility with specific experimental platforms. For example, fabrication of such untethered and mechanically strong neural tissue mimics (NTMs) could help in the assessment of new electrodes for neural functionality, neurotransmission, and the assessment of biocompatibility and neural damage during implantation (15–17). On the other hand, efforts to develop freestanding 3D tissue models in vitro that incorporate neuronal functionality, such as the formation of neuromuscular junctions in 3D muscle tissues, are limited when trying to adhere the neurons on the overall 3D constructs (12, 18). Having control of the size and geometry of a NTM that can be handled and installed after neural development can facilitate the assembly of neurodriven biological machines (19). Furthermore, continued advancements toward engineered in vitro neural tissues of various shapes and sizes to develop better models are important to minimize the use of animal models (20) (Fig. 1C).

In this work, we utilized fibrin as a scaffold to engraft differentiated embryonic stem cell (ESC)-derived neurons prior to their maturation in order to achieve untethered and geometrically stable NTMs that could be molded into desired shapes. We demonstrated and characterized three shapes: a rod, a cube, and a toroid (Fig. 1B and *SI Appendix*, Fig. S1). By using mouse ESCs, we compared seeding cell densities to determine a protocol for tissue formation of various shapes. We also characterized development and functionality, first using mouse-derived ESCs (mESCs) due to their shorter differentiation times and reduced costs compared to human stem

Significance

Forward design of tissue-like structures is very important for biomedical and engineering applications. We developed a methodology for designing 3-dimensional (3D) neural tissue mimics that can be formed into desired shapes and sizes, while maintaining their electrical functionality, and can be physically transferred to different platforms. These biofabricated neural constructs could facilitate assembling biological machines, advance methods for assessment of neural functionality in vitro, and support the development of improved models for disease studies.

www.manaraa.com
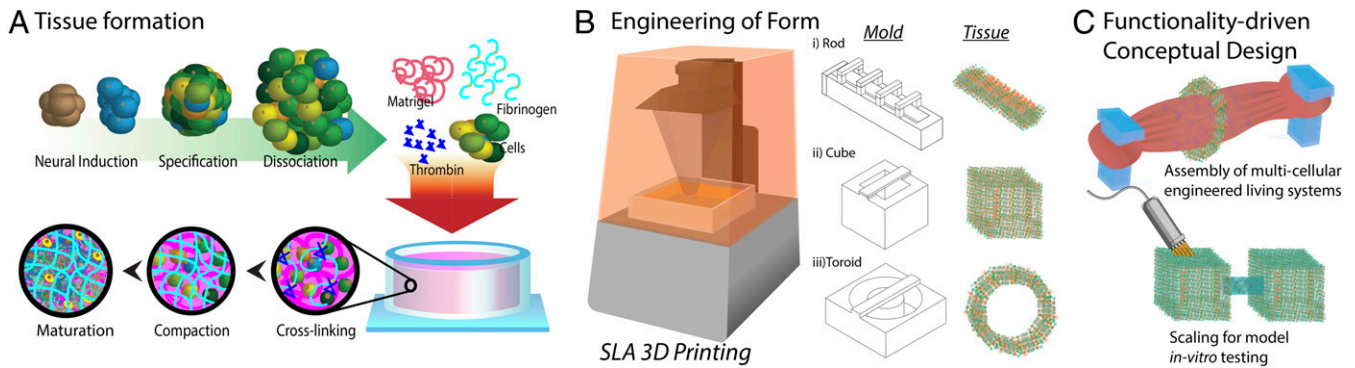
Fig. 1. Development of 3D neural tissue mimic (NTM) for biomedical engineering applications. (*A*) Representative schematic of the NTM formation, consisting of differentiation, dissociation, and engrafting of differentiated neurons in fibrin hydrogel prior to maturation. (*B*) Diagram of SLA 3D printer used for the fabrication of the 3 molds used to form different neural constructs: rod, cube, and toroid. (*C*) Representation of possible biomedical applications that could benefit from control of the shape and size of neural tissue models.

cells. We then implemented the protocol with human stem cells to demonstrate the possibility for clinical and biomedical applications.

Results and Discussion

Seeding Cell Density Affects the Structure of the NTM. Previous works have studied the effects of changing the stiffness of the fibrin matrix on the resulting viability of tethered NTMs by changing the concentration of fibrinogen with respect to the added thrombin (21–23). We build upon those studies, but due to our desire to obtain mechanically stable and untethered functional 3D in vitro constructs, we studied the effect of varying the seeding cell concentration. For the purpose of our study, the day in which seeding took place was labeled as D0 (*SI Appendix*, Fig. S2). Prior work on developing untethered muscle tissue has reported 5e6 myoblasts per mL as the optimal cell seeding concentration (7, 24). Due to the lower traction force per neurons compared to myoblasts, we considered higher seeding cell concentrations (25). The goal was to find a cell concentration that would result in a mechanically strong structure while being low enough to lower costs and have high sample throughput. For this purpose, we studied 5e6 cells per mL (1×), 12.5e6 cells per mL (2.5×), 25e6 cells per mL (5×), and 50e6 cells per mL (10×) and observed them for the first 4 d of compaction (*SI Appendix*, Fig. S3 and Movies S1–S4). It was noticed that by D1 for all 4 concentrations, neurites were extending across the fibrin hydrogel. However, for higher concentrations (5× and 10×), dark clusters started to form by D4 (Fig. 2*A*). This spontaneous reaggregation toward neural clumps could lead to heterogeneity across the tissue mimic, and if the clusters become too large could also lead to necrosis due to diffusion limitation (26). To investigate the difference in NTM architecture, we measured high-resolution confocal *z* stacks of the resulting constructs at the 4 seeding densities stained for β-tubulin III, a general neural microtubule marker (Fig. 2*B*). These images showed that higher seeding cell densities caused the cells to recluster as EBs and extend processes in clumps rather than homogenous neurite extensions, as also seen clearly in the frequency domain (Fig. 2*C*). Due to the desire to achieve a homogenous internal environment to avoid the risks of clustering and optimize the consistency across the construct, we further quantified these trends in heterogeneity. For this purpose, the randomness of the images was measured using the MATLAB function for entropy, *e*, defined as follows: $e = -\sum p(z_i) * \log_2 p(z_i)$, where *p* contains the normalized histogram counts of the field of view, z_i (27) (Fig. 2*C*). We observed that the randomness of the neurite structures was higher for lower concentrations and decreased significantly for 10× cell concentration. To further understand these observations, we performed continuous live quantitative phase imaging using gradient light interference microscopy, which allows for a label-free method to estimate the dry cell mass, i.e., the protein content of the cells (28). The rates were statistically insignificant across the groups (Fig. 2*D*), hinting that the possible mechanisms for the difference are due to the reorganization of the NTM rather than the cellular growth itself.

Seeding Cell Density Affects the Compaction and Neurite Extension of the NTM. We first utilized the rod-shaped NTM and observed the effects of cell density on the compaction of the construct when seeded in the PEGDA molds, and later, the neurite extension from the compacted NTM when cultured after compaction. Upon seeding, we measured the dimensions of the compacted NTM for the 4 concentrations being tested with respect to the size of the mold, to which the cell-hydrogel solution mimic initially conformed during the stage prior to cross-linking (Fig. 3*A* and *SI Appendix*, Fig. S4). We observed that, for the lower 1× concentration, the percent decrease compared to the original dimension was below 10% by D4 for both the width and the length of the rod (Fig. 3*B*). This translated in difficulty of handling the 1× NTMs as they would rupture very easily. When the cell concentrations were increased to 2.5× and 5× concentrations, the width decreased approximately by 30% and 40%, respectively, and the length decreased by ~50% for both. Interestingly, the highest seeding density showed the least compaction, which could possibly indicate reaching a saturation of cells within the mold volume. NTMs from each group were placed at D4 on functionalized substrates in order to observe the neurite extension, as it was important to ensure that these neural constructs were able to innervate and communicate with downstream biological structures. For this reason, we measured length and number of neurites extending across the periphery of the neural construct. (Fig. 3*C*) After 2 d of the NTM being adhered, we observed numerous processes extending from the NTM beyond an initial sheet of membrane layer directly connected to the NTM. We observed that, for lower seeding concentrations, the neurite length reached around 2 mm and significantly decreased for constructs of larger cell concentrations (Fig. 3*D*). Next, the number for neurites extending from the NTM was measured by plotting the cross-sectional profile and counting the peaks (Fig. 3*E*). The neurite numbers significantly increased between 1× and 2.5×, and then stayed constant for the subsequent concentrations. The fact that the 3 highest concentrations seemed to have similar neurite counts, while having such differences in neurite length, could be related to the observed internal clustering of cells (Fig. 2*C*). While observing the neurite extension over a longer period of time, beyond the second day of adhesion (D6+), would have been even more useful, we did observe neurons migrating from the NTM and into the substrate, extending their own processes, and making it hard to distinguish from processes directly
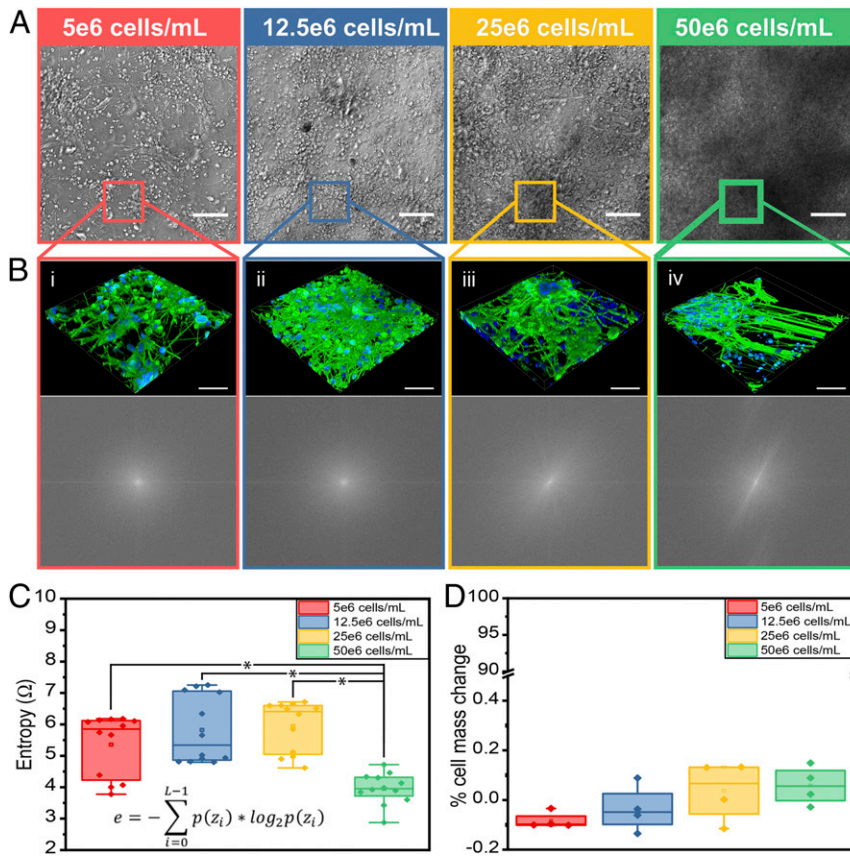
Fig. 2. Cell seeding density affects homogeneity of internal neuronal architecture of NTM. (*A*) Phase contrast image of the neurons engrafted in fibrin hydrogel at D4 of compaction after neural construct formation for the different seeding cell densities from D0: 5e6 cells per mL, 12.5e6 cells per mL, 25e6 cells per mL, and 50e6 cells per mL. (Scale bar: 50 μm.) (*B*) 3D rendering of confocal *z* stacks across 15 μm of neurites (β-TubIII: green) and nuclei (DAPI: blue), with the corresponding representation in the frequency domain obtained through fast Fourier transform for the 4 cell seeding densities. (Scale bar: 20 μm.) (*C*) Entropy of neurite alignment for 4 seeding densities at D4 ($n = 12$, *$P < 0.05$, ANOVA with Tukey's post hoc). (*D*) Cell dry mass change for the 4 seeding densities between D0 and D4 ($n = 4$).

The entropy equation shown in panel C:
$$e = -\sum_{i=0}^{L-1} p(z_i) * log_2 p(z_i)$$

extending from the NTM. Nevertheless, these observations led us to select 12.5e6 cells per mL (2.5×) as an appropriate concentration for the rest of the study.

NTMs Can Be Molded into Various Shapes. Upon establishing a reproducible cell culture protocol, we then fabricated molds of different shapes to confirm that mechanical stability observed in the rods would be preserved in other shapes. First, a cube was designed by adjusting the dimensions of the mold to keep the seeding volume constant as the rod design earlier (Fig. 4*A*). A similar compaction trend was observed for these cubes, where original volume decreased by ∼60 to 70% (Fig. 4*B*). To show a possible applicability of cube-shaped NTMs for developing 3D neural circuits, we fabricated a holding mold with slits between the enclosures in which to place the compacted cubes. The goal was to add ECM around the cubes and observe whether the cubes would extend processes across it (Fig. 4*C*). After 4 d of "installation," the cubes were observed to localize toward the center, which would be explained by remodeling of the ECM as neurites extend across and pull on each other. We confirmed by confocal imaging the presence of dense extension of processes between the slits.

In parallel, a mold for a toroid was fabricated in order to obtain a neural ring (Fig. 4*D*). The compaction process here was different, as a solid structure held the inner diameter constant, while the outer diameter decreased due to the cell-driven hydrogel compaction, resulting in the thickness decrease by ∼60% (Fig. 4*E*). This shape was especially significant as it proved that the formation of NTMs by these protocols resulted in stable geometries, even if the NTM was cut in half (*SI Appendix*, Fig. S5). Furthermore, because the compaction occurred while an external structure kept the cell-matrix liquid, we hypothesized that the structures could be removed and installed onto a cylindrical structure, and (because of the built-in tension), would fit "tightly" (Movie S5). Using Lightsheet

microscopy, we observed that installed rings not only fitted tightly around the cylindrical substrate but also extended a dense mesh of processes (Fig. 4*F*).

Maturation within the Exogenous ECM Supports Development of Neural Populations. When presenting this tissue model as a substitute for intact EBs for neural studies, we wanted to determine the effect of disrupting EB cells and then reconstructing them in an exogenous matrix. For this purpose, we focused on common neural populations such as excitatory and inhibitory phenotypes, as well as motor neurons and supporting populations such as astrocytes and oligodendrocytes. Initially, we performed confocal imaging of NTM slices and observed that between D4 and D7, neural populations seemed to be developing as expected (29–31) (Fig. 5*A*). The staining for vesicles of the excitatory neurotransmitter, glutamate, showed a wider propagation of these markers across the slice, while markers that stained for the enzymes responsible for synthesis of GABA, a primary inhibitory neurotransmitter, did not show any significant signal. Motor neurons were monitored through the ChAT stain and showed an increase in ChAT+ neurons across the slice between D4 and D7, an observation that was similar for the astrocytes and oligodendrocytes stained for GFAP and CNPase, respectively. These observations were confirmed and quantified by qPCR and normalized for comparison across targets with respect to the housekeeping gene GAPDH using standard curves (*SI Appendix*, Fig. S6). We compared 3 known targets for excitatory populations: ADORA2a (AD), Grin1 (GR), and TH; 2 targets for inhibitory populations: PVALB (PA) and GAD1 (GA); 2 targets for motor neurons: MNX1 (MN) and ChAT (CH); and 2 targets for supporting cells: GFAP (GF) and CNPase (CN) (Fig. 5*B*). At D0, as expected, MN is expressed various fold higher than most other markers as it is the transcription factor for the differentiation of motor neurons. By D4, MN still expressed highly (with respect to other
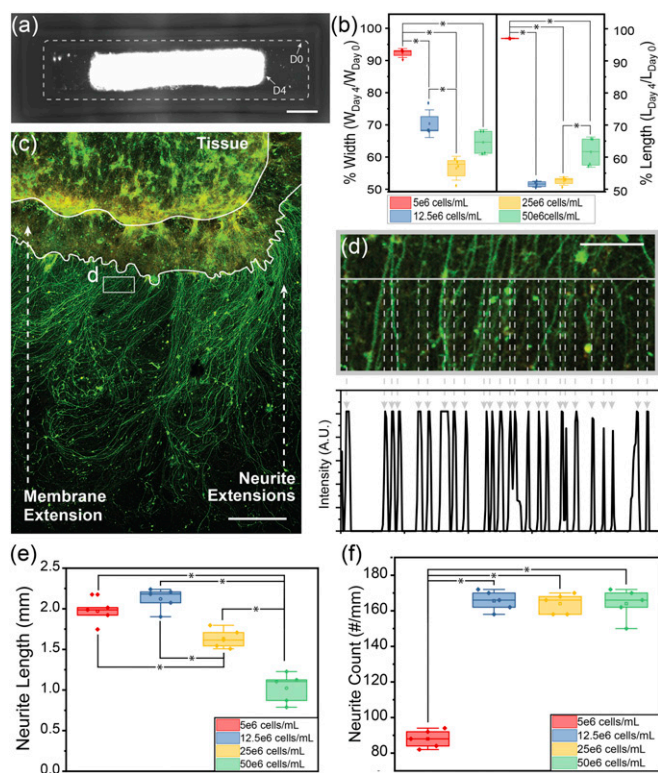
Fig. 3. Cell seeding density affects compaction and neurite extension from the neural tissue mimic (NTM). (*A*) Representative fluorescent image of a compacting NTM (rod) in the mold at D4. (Scale bar: 1 mm.) (*B*) Percent change of the width ($Width_{D4}/Width_{D0} \times 100$) and length ($Length_{D4}/Length_{D0} \times 100$) of NTMs (rods) resulting from the 4 cell seeding densities ($n = 5$; *$P < 0.05$, ANOVA with Tukey's post hoc). (*C*) Representative confocal image of tissue seeded on functionalized substrate showing neurite extension from the NTM (β-TubIII, green; F-actin, red). (Scale bar: 500 μm.) (*D*) Zoom of neurites from *C* across the perimeter of the NTM. Fluorescent intensity profile was used to detect and count neurites. (Scale bar: 50 μm.) (*E*) Length of neurites extending from the membrane extension from the NTM for the 4 cell seeding densities ($n = 5$; *$P < 0.05$, ANOVA with Tukey's post hoc). (*F*) Number of neurites per millimeter of NTM perimeter for the different cell seeding densities ($n = 5$; *$P < 0.05$, ANOVA with Tukey's post hoc).

markers) while CH also expressed highly, indicating maturation of the motor neurons, as CH is critical in the synthesis of the motor neuronal neurotransmitter, acetylcholine. Furthermore, GR, a gene that encodes for the receptor for excitatory neurotransmitter glutamate, became highly expressed, while the high expression from D0 of TH, which encodes for dopamine-synthesizing enzymes in dopaminergic neurons, showed to be only transient. Prior studies have shown this to be a common occurrence in many developing neurons from the central nervous system (32, 33). More importantly, expression of astrocytes and myelinated oligodendrocytes also increased, almost as much as that of functional motor neurons. On D7, the same trends from D4 were observed; however, the expression of the supporting cells surpassed the expression of other markers. Since both astrocytes and oligodendrocytes are mitotic while neurons are generally considered to be amitotic, it would be worth considering how a large neuron-to-glial ratio would affect 3D culture viability and how this would affect the lifetime of these NTMs. Nevertheless, we also observed the same expression of markers during development in intact EBs that were grown in parallel (*SI Appendix*, Fig. S7). We then compared these observations between NTM and EBs for the targets that reported cycle threshold (Ct) values above 35 by D7 (*SI Appendix*, Fig. S8). When both NTM and EBs were compared at D4 and D7 with respect to predissociation EBs at D0, no significant differences were found for

almost any of the markers at both days of study (Fig. 5*C*). This served as an indication that the initial disruption and reconstruction of a foreign ECM did not affect the differentiation and development of general neuronal populations. While this initially was surprising, given the constructs' millimeter-scale sizes, which greatly surpassed the EB size and were past the diffusion limit for most tissues, upon imaging the tissues through a scanning electron micrograph, we observed that the ECM on the outside had pores that were much larger than macromolecules in the media. This would indicate that nutrients were able to diffuse in and out of the tissue (*SI Appendix*, Fig. S9).

Finally, hematoxylin and eosin stains were performed in histology slices to determine the distribution of cells within the NTM (Fig. 5*D*). After processing the images, they were segmented in 200×200-μm-sized bins and cells were counted within each bin to have a spatial notion of local cell concentrations (Fig. 5*E*). Upon observation, it was apparent that cells, while still alive and distributed across the NTM (which was clear by close inspection of the histology slices), would concentrate closer to the edges, and 75% of all cells seemed to be distributed within the first 150 μm from the edge. Furthermore, quantifying the expression of the principal ECM proteins in primary neural tissue and comparing between the intact EBs and the in vitro NTM showed again no significant disruption of expression during development (34–37) (*SI Appendix*, Fig. S10). These observations would suggest that the fabrication of in vitro NTM as demonstrated by this work could serve as a model to study various developmental phenomena despite the disruption of EB development during the formation of the 3D neural constructs.

In Vitro Neural Tissue Mimic Develops Spontaneous Electrical Activity and Shows Spatial Connectivity. While we are able to control the form and shape of the NTM, the electrical functionality must also be validated. Multiple studies of EBs differentiated to various neuronal phenotypes have shown the development of spontaneous electrical activity (38–40). To assess the electrical activity, the NTMs were placed on functionalized microelectrode arrays (MEAs). The electrodes that recorded the most activity were directly under the NTM compared to electrodes away from the construct (Fig. 6*A*). This activity was quantified primarily by the spike rate and was shown to gradually increase with time, as expected for maturing neural networks (Fig. 6*B* and *SI Appendix*, Fig. S11). Synchronized bursting can be appreciated by the spike raster plots, which showed some random firing from various outside electrodes from migrating neurons but showed structured firing for the electrodes that were under the NTM (Fig. 6*C*). Furthermore, quantifying synchronicity of the firing by calculating the average cross-correlation values per electrode with respect to the rest of the electrodes showed synchronous behavior across the length of the construct (Fig. 6*D* and *SI Appendix*, Fig. S12).

Given the conventional perspective that "neurons that fire together, wire together," we inferred that the synchronous bursting observed in the spontaneous activity should indicate a strong connectivity across the tissue. To prove this, we formed NTMs from optogenetic mESCs, placed the construct on the MEA after compaction, and used a focused light with a small spot size (~2.5 mm) to stimulate the section of the NTM that was not on the MEA sensing area. This experiment was performed for the rod and the toroid, as the cube dimensions did not allow for the stimulation to be done only on sections that were removed from the recording electrodes (Fig. 6*E*). The average firing rates of the 20-s intervals corresponding to before, during, and after stimulation were mapped to their respective electrodes (Fig. 6*F* and *SI Appendix*, Fig. S13). During stimulation away from the measuring electrodes, an increase in firing rate clearly indicates that the processes are electrically connected across the entire NTM. As expected, there would be some variation in the response as the interface between the construct and the measuring electrodes might not be identical and hence result in a

ENGINEERING
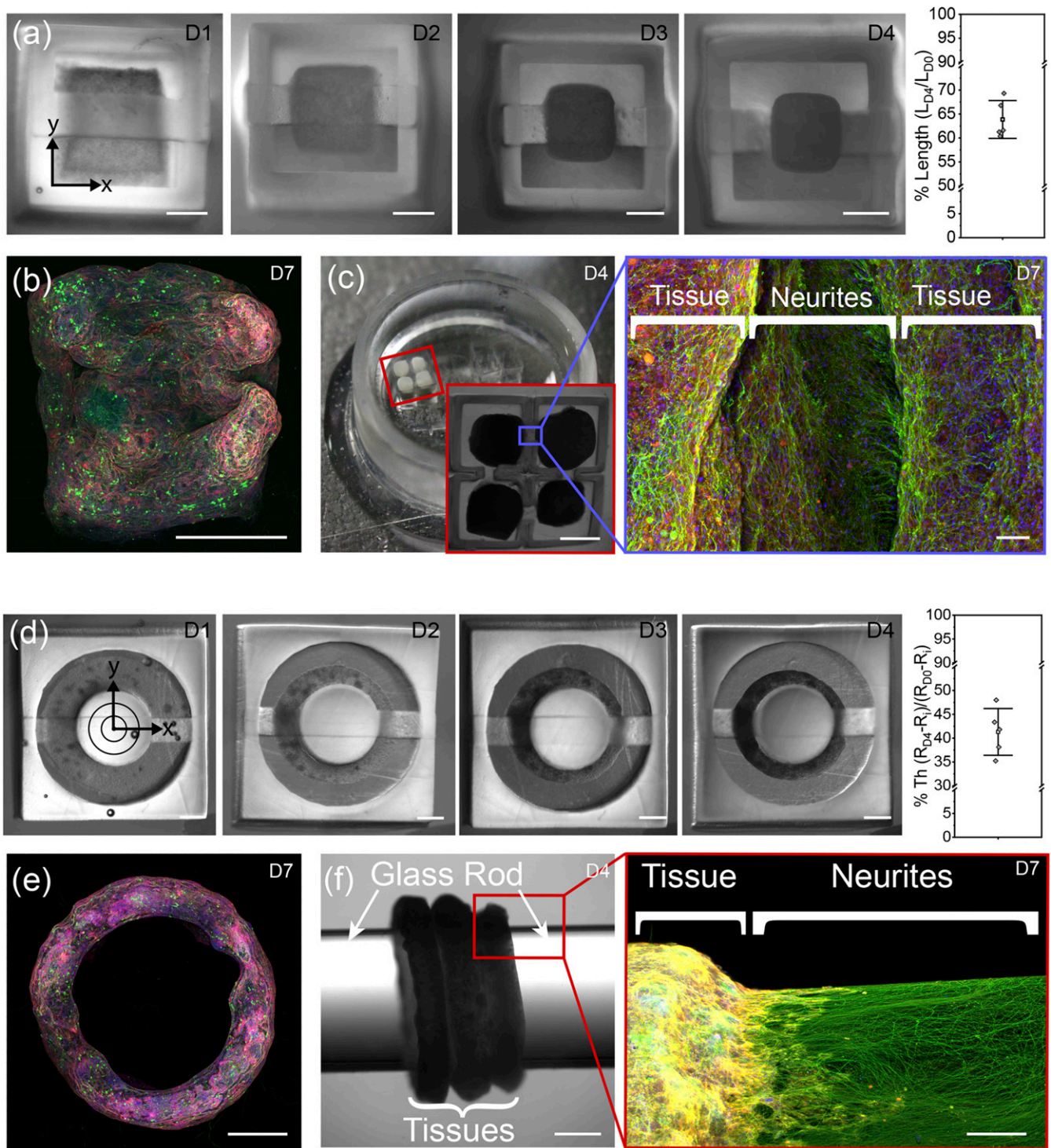
Fig. 4. Formation of neural tissue mimics (NTMs) of different shapes. (*A*) Compaction of cube-shaped construct during the first 4 d, and percent change of side length [(Average Length at D4)/(Average Length at D0) × 100]. (Scale bar: 1 mm.) (*B*) Confocal of compacted cube NTM. (Scale bar: 500 μm.) (*C*) Installation of cube NTMs (D4) on 3D printed holders embedded in Matrigel solution after compaction in the molds. To the *Right*, confocal image of neurites extending between 2 installed cube NTMs. (Scale bar: 1 mm; 50 μm.) (*D*) Compaction of toroid-shaped NTM during the first 4 d, and percent change of thickness [(Outer Radius at D4 – Inner Radius)/(Outer Radius at D0 – Inner Radius) × 100]. (Scale bar: 1 mm.) (*E*) Confocal of compacted toroid NTM. (Scale bar: 1 mm.) (*F*) Installation of toroid NTMs (D4) on functionalized glass cylinders after compaction in the mold. To the *Right*, a LightSheet image of neurites extending throughout the glass rod (β-TubIII, green; F-actin, yellow). (Scale bar: 1 mm; 500 μm.)

difference in the magnitude of the measured signal. This stimulation was repeated 4 times for 2 samples of each shape, and the average firing rate for all of the electrodes showed a consistent increase in activity from electrodes away from the stimulation

(Fig. 6*G*). Using a small spot size and stimulating the rod and the toroid on a section of the neural construct away from the electrodes and still detecting the evoked response at the electrodes proved that these NTMs were not only spontaneously active but
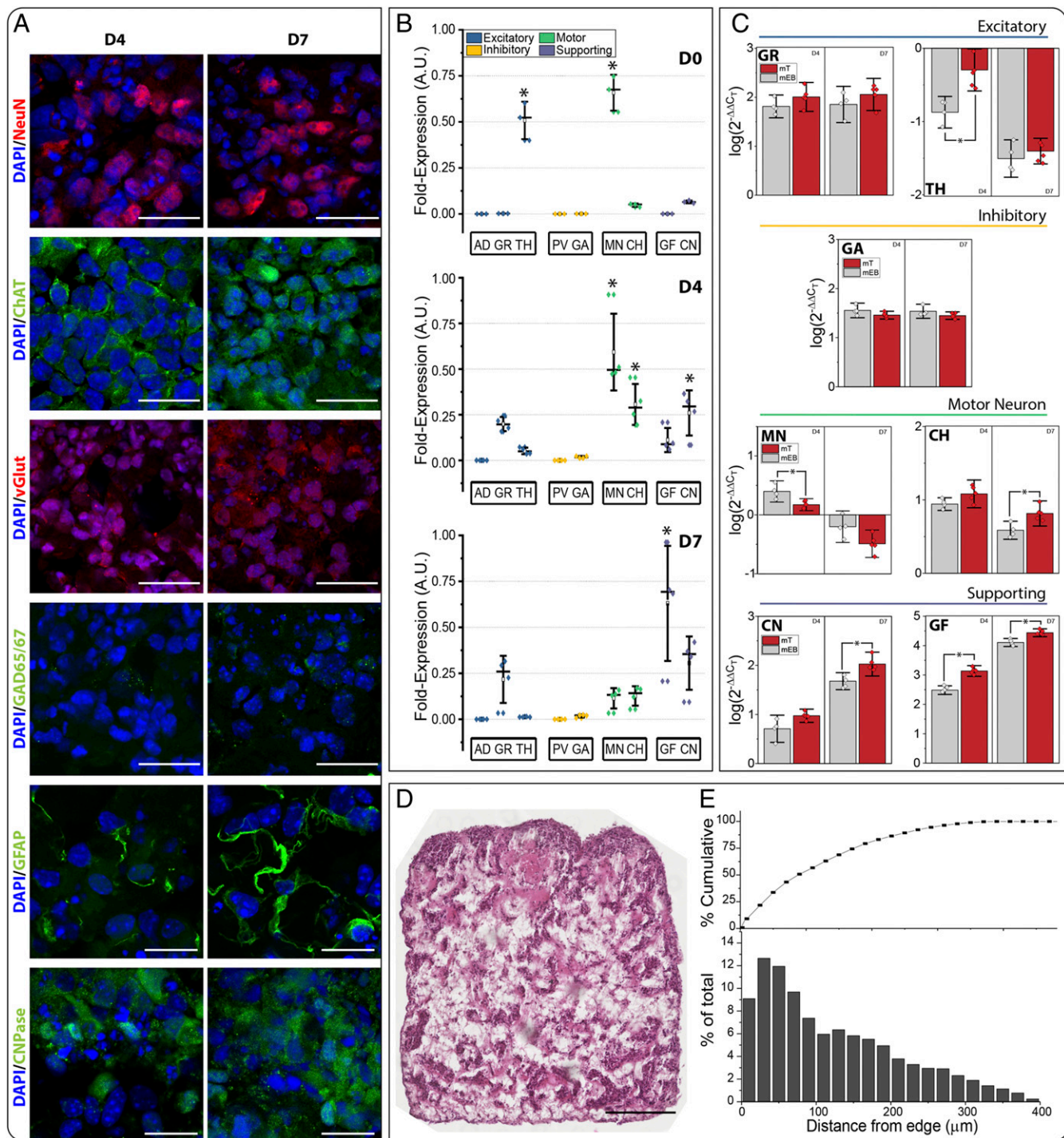
Fig. 5. Engrafting neuronal populations within fibrin hydrogen did not disrupt phenotypical maturation. (*A*) Confocal images of 5-μm-thick cryosections for key neural populations at D4 and D7. (Scale bar: 25 μm.) (*B*) Fold expression of RNA expression across normalized population targets with respect to housekeeping gene, GAPDH, for D0, D4, and D7 (*n* = 5) (targets for excitatory neurons [blue]: AD, Adora2a; GR, Grin1; TH, tyrosine hydroxylase; targets for inhibitory neurons [yellow]: PV, parvalbumin; GA, Gad1; targets for motor neurons [green]: MN, Mnx1; CH, ChAT; targets for supporting cells [purple]: GF, GFAP; CN, CNPase). (*C*) Comparison between mouse EBs (gray) and NTMs (red) of RNA expression for the population targets with $Ct_{adj} < 35$ at D7 and with respect to GAPDH, normalized to D0 ($n_{MEB} = 4$, $n_{mT} = 5$; *$P < 0.05$, *t* test). (*D*) Histology of NTM slices at D7. (Scale bar: 200 μm.) (*E*) Histograms of cell position from the nearest edge of the slice, shown in cumulative percentage (*Top*) and percentage of total per 20-μm bins (*Bottom*).

also forming connected networks that extended across the NTM geometry.

NTM Formation with Human ESCs. While utilization of mESCs can still provide an experimental platform for many studies within tissue engineering research, the demonstration of alternative biofabrication methods in human-derived stem cells is highly attractive for the development of translational research models. Using the protocol described earlier in this paper, human ESC (hESC)-derived neural cubes were fabricated (41–43) (Fig. 7*A*). For these NTMs, the same cell

Pagan-Diaz et al.

www.manaraa.com
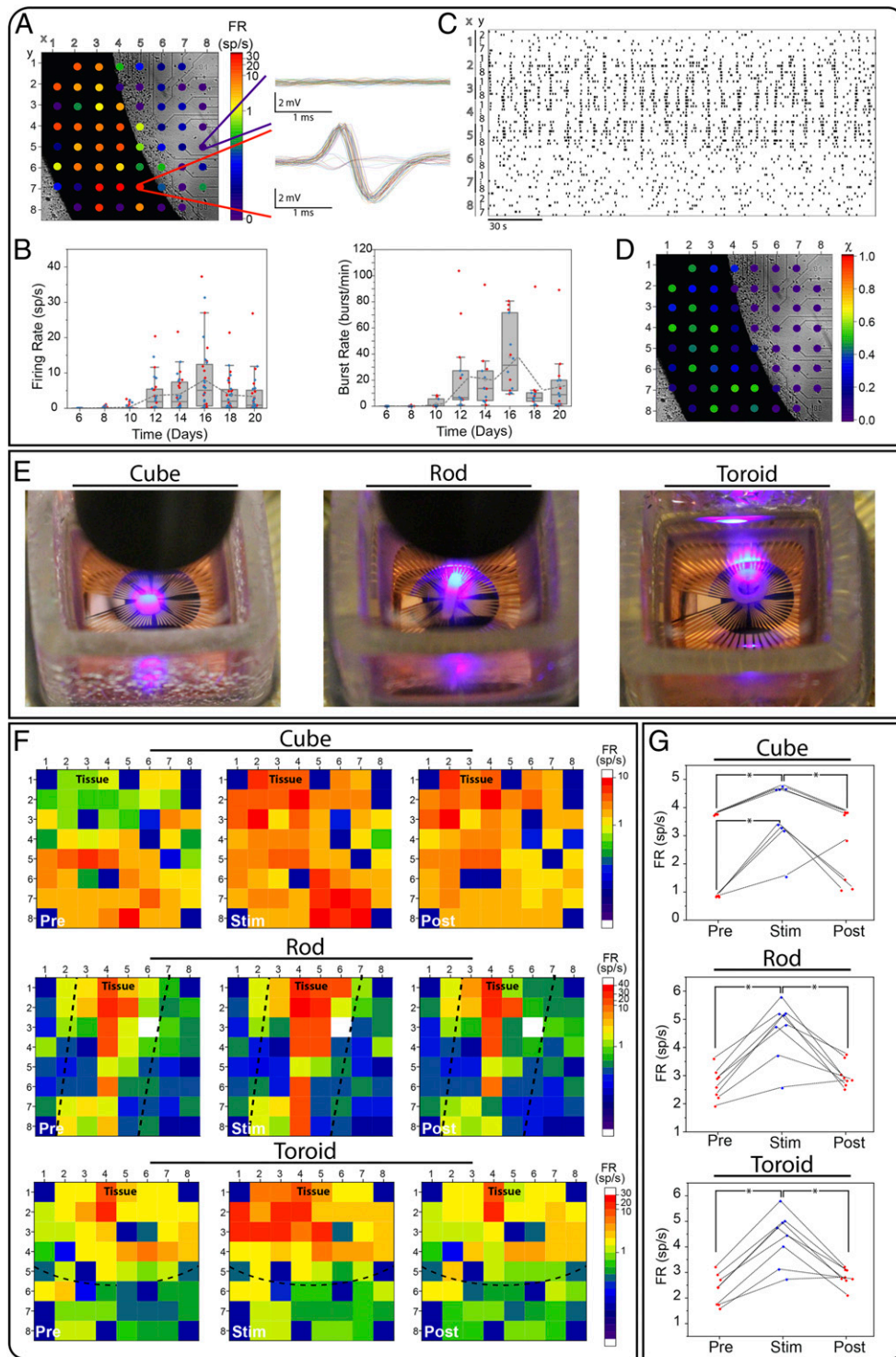
Fig. 6. Optogenetic neural tissue mimics (NTMs) are spontaneously active and also develop connectivity across the construct. (*A*) Phase contrast image of a rod NTM on an MEA with electrodes colored for the corresponding averaged measured firing rate (FR) (spike [SP]/s) for D16. Expansions show overlay of all action potentials recorded in 2 s for an electrode far from the NTM (*Top*) and an electrode directly under the NTM (*Bottom*). (*B*) Firing spike and burst rate for 20 highest recording electrodes for 2 NTM samples (red and blue) across 16 d (installed on MEA at D4, started recording 2 d later). (*C*) Raster plot showing active seconds (seconds where electrodes recorded activity) across all electrode channels for rod NTM for D16. *Left* legend corresponds to electrode position. (*D*) Phase contrast image of a rod NTM on an MEA with electrodes colored for the corresponding averaged cross-correlation value normalized to unity for D16. (*E*) Representative image of focused stimulating incident beam size on the NTM with respect to the section of the structure that is over the recording electrodes for the cube (*Top*), rod (*Middle*), and toroid (*Bottom*). (*F*) Matrix showing firing rate per electrode, where each element corresponds to each electrode on the MEA for the cube (*Top*), rod (*Middle*), and toroid (*Bottom*). Matrix on the *Left* corresponds to the average firing rate during 20 s prior to stimulation, matrix in the *Center* corresponds to the firing rate during 20 s of pulsed stimulation illuminated in the section of the NTM farthest from the sensing electrodes (for rod and ring), and matrix on the *Right* corresponds to the average firing rate during 20 s after stimulation. (*G*) Firing rate prior (Pre; red), during (Stim; blue), and after (Post; red) stimulation for 4 stimulation repetitions done on 2 separate NTMs for the 3 shapes: cube (*Top*), rod (*Middle*), and toroid (*Bottom*) ($n_{Cube} = 4$, $n_{Rod\ and\ Toroid} = 8$; *$P < 0.05$, ANOVA with Tukey's post hoc).

www.manaraa.com

seeding concentration used for the mouse NTM were mixed with the protein solution used previously and poured into the mold. These NTMs proceeded to compact, showing similar percent volume decrease as the mouse-derived NTMs (Fig. 7B). Furthermore, histology sections showed again similar cell distribution patterns as seen for the mouse-derived NTMs and effective differentiation of excitatory neuronal populations as shown by positive staining of vGlut (44) (Fig. 7C and *SI Appendix,* Fig. S14). Moreover, we placed and seeded hESC-derived NTMs on MEAs to validate spontaneous activity from the neural constructs (Fig. 7D and *SI Appendix,* Fig. S15). These human-derived constructs showed spontaneous bursting along the action potential firing (Fig. 7E). More importantly, we measured the response to known neural antagonists from the seeded NTMs. Following MEA studies with hESC-derived neuronal cultures, spontaneous activity was measured followed by the addition of D-AP5 (30 μM), an NMDA receptor antagonist, followed by a washout to determine whether the samples would return to baseline firing (40). Afterward, the inhibitory neurotransmitter GABA was added (100 μM), followed by the GABA receptor antagonist bicuculine (30 μM). The firing rate responded as expected: Addition of D-AP5 decreased the firing rate with respect to the spontaneous activity and returned back when washed away (Fig. 7F). When GABA was added, a more acute inhibitory response was observed, only to reverse upon the addition of bicuculine. Furthermore,

effects to these drugs were also observed in the bursting (Fig. 7G). Several electrodes had been recording spontaneous bursting, and dissipated when adding the NMDA receptor antagonist, D-AP5, and the inhibitory neurotransmitter GABA. Both washing away the D-AP5 and blocking GABA receptors with bicuculine, resulted in the return of this bursting phenomena, with the latter increasing the number of bursts being recorded. However, while bicuculine did cause more than a 2-fold increase of the number of bursts recorded, observing the structure of the burst themselves, there seemed to be no significant difference between the burst duration (Fig. 7H) or the spike frequency within the burst (Fig. 7I). These observations led us to conclude that these NTMs could be utilized in translational studies while also taking advantage of the capability of molding the neural constructs in the desired shapes for optimized bottom-up experimental design.

Conclusion

This work demonstrated the fabrication of untethered functional NTMs that can be molded into a variety of 3D shapes and sizes. mESC-derived neurons, when mixed with fibrin and ECM and allowed to differentiate in a 3D printed mold, resulted in a compaction of the cells and matrix. This ultimately resulted in a NTM that did not perturb the development of the neural populations when compared with the standard environment of the EB while
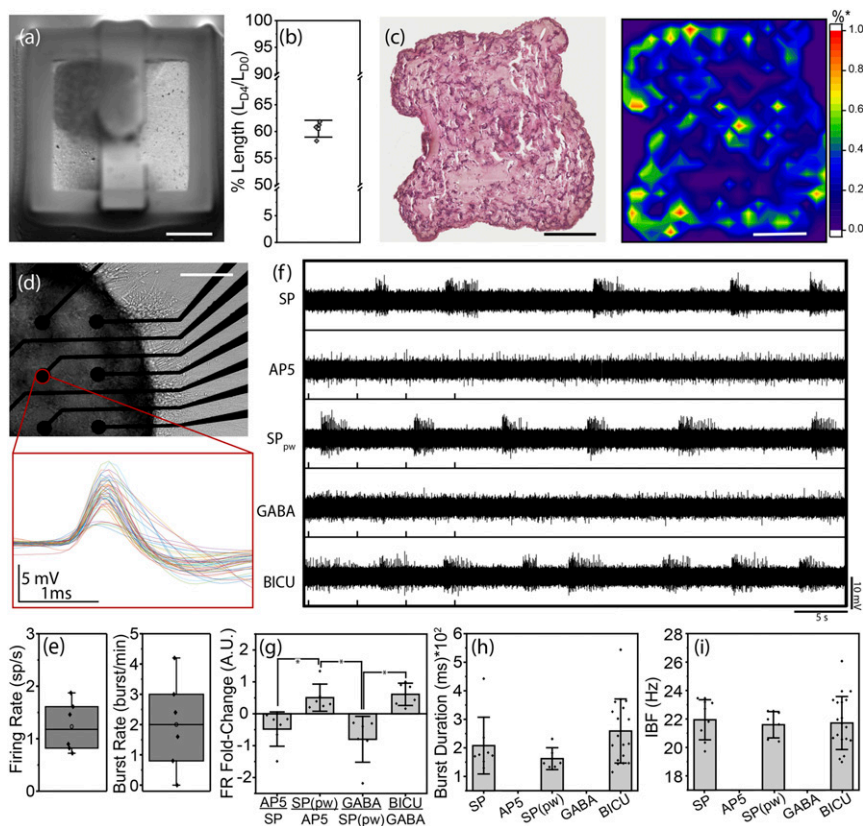
Fig. 7. hESC-derived neural tissue mimics (NTMs) compact similar to mESC-derived and respond to drugs. (A) Compacted cube NTM formed from hESCs at D4. (B) Percent of compaction of the sides [(Average Length at D4)/(Average Length at D0) × 100] ($n = 4$). (Scale bar: 1 mm.) (C) Histology of hESC-derived NTM slices at D10 alongside percent of cell count in 100-μm bins to total cell count from histology slices, normalized to 1 [%$_i$ = Cell Count in Bin$_i$/Total Cell Count; %* = %$_i$/max(%$_i$)]. (Scale bar: 200 μm.) (D) hESC-derived cube NTM on MEA, extending processes with representative action potentials recorded from spontaneously firing. (Scale bar: 200 μm.) (E) Average spike and burst rate during recording of spontaneous activity at D10. (F) Representative electrode recording for NTMs firing in different conditions (*Top* to *Bottom*): spontaneous, D-AP5, spontaneous post-washout, GABA, and bicuculline. (G) Fold change of average firing rates across active electrodes ($\log[FR_{post}/FR_{pre}]$) for 6 samples between post and pre states corresponding to either addition of drug or washes (AP5:SP → firing rate after adding D-AP5 with respect to the spontaneous firing rate; SP$_{pw}$:AP5 → firing rate after washout with respect to the firing rate during the presence of D-AP5; GABA:SP$_{pw}$ → firing rate after adding GABA, with respect to the firing rate post washout; BICU:GABA → firing rate after washing out GABA and adding bicuculine, with respect to firing rate during the presence of GABA) ($n = 6$; *$P < 0.05$, t test). Effect of drugs on bursting was evaluated for the recorded bursts through (H) burst duration and (I) spike frequency within each burst.

Pagan-Diaz et al.

overcoming geometrical limitations of the spherical EB, which at many times restricts experimental design and applications. By providing this reproducible protocol to obtain dense and modular neuronal tissue models, development of platforms to assess neural function in 3D can be advanced, since electrophysiological activity and connectivity that extended across the NTM were demonstrated. Finally, we validated our protocol with human stem cell-derived neurons to achieve these functional NTMs. These findings could be enhanced by expanding control of the biofabrication protocol to include higher precision of neuronal population ratios as well as patterning these populations in 3 dimensions in order to achieve phenotype-specific spatial arrangements and functionality as found in vivo tissues. The ability to recapitulate neural morphology, both internally and externally, could improve translational applicability as well as present a better model for the study of emergence of neurological phenomena. Overall, these NTMs can have profound applications in drug discovery and screening, as biomedical neural implants, and use in biological robotics and engineering applications.

Methods

Optogenetic mESC line ChR2H134R-HBG3 Hb9-GFP (27), generously gifted by Prof. Roger Kamm from Massachusetts Institute of Technology (Cambridge, MA), and hESCs (H9) (WiCell, WA09) were cultured and differentiated following

established protocols (44, 45). Molds were fabricated using a 3D printed using a SLA Asiga Pico 2 (Asiga) and following standard protocols provided by the company, and were sterilized through a sequential bath of bleach, IPA, and PBS, prior to UV illumination. Tissue mimic seeding was performed by embedding dissociated EBs in a mixture of fibrinogen, thrombin, and Matrigel (Corning). Electrophysiological studies were performed using functionalized 60-electrode chip using a MEA 2100-Lite Amplifier (Multi Channel Systems MCS) for recording and a laser diode with an integrated driver set at 450 nm (Doric Lenses) for stimulation. Further details of our experimental methods can be found in *SI Appendix*.

Data Availability. All of the information required to reproduce this work is contained in this paper. Any material, raw data, and analytical tool utilized in this study are available by the authors upon request.

1. B. Tian *et al.*, Macroporous nanowire nanoelectronic scaffolds for synthetic tissues. *Nat. Mater.* **11**, 986–994 (2012).
2. P. Bajaj, R. M. Schweller, A. Khademhosseini, J. L. West, R. Bashir, 3D biofabrication strategies for tissue engineering and regenerative medicine. *Annu. Rev. Biomed. Eng.* **16**, 247–276 (2014).
3. R. D. Kamm, R. Bashir, Creating living cellular machines. *Ann. Biomed. Eng.* **42**, 445–459 (2014).
4. R. M. Duffy, A. W. Feinberg, Engineered skeletal muscle tissue for soft robotics: Fabrication strategies, current applications, and future challenges. *Wiley Interdiscip. Rev. Nanomed. Nanobiotechnol.* **6**, 178–195 (2014).
5. M. Thomas, S. M. Willerth, 3-D bioprinting of neural tissue for applications in cell therapy and drug screening. *Front. Bioeng. Biotechnol.* **5**, 69 (2017).
6. L. Ricotti *et al.*, Biohybrid actuators for robotics: A review of devices actuated by living cells. *Sci. Robot.* **2**, eaaq0495 (2017).
7. C. Cvetkovic *et al.*, Three-dimensionally printed biological machines powered by skeletal muscle. *Proc. Natl. Acad. Sci. U.S.A.* **111**, 10125–10130 (2014).
8. S. G. M. Uzel *et al.*, Microfluidic device for the formation of optically excitable, three-dimensional, compartmentalized motor units. *Sci. Adv.* **2**, e1501429 (2016).
9. R. Raman *et al.*, Damage, healing, and remodeling in optogenetic skeletal muscle bioactuators. *Adv. Healthc. Mater.* **6**, 1700030 (2017).
10. J. B. Black, P. Perez-Pinera, C. A. Gersbach, Mammalian synthetic biology: Engineering biological systems. *Annu. Rev. Biomed. Eng.* **19**, 249–277 (2017).
11. W. J. Polacheck, C. S. Chen, Measuring cell-generated forces: A guide to the available tools. *Nat. Methods* **13**, 415–423 (2016).
12. Y. Morimoto, M. Kato-Negishi, H. Onoe, S. Takeuchi, Three-dimensional neuron-muscle constructs with neuromuscular junctions. *Biomaterials* **34**, 9413–9419 (2013).
13. J. A. Umbach, K. L. Adams, C. B. Gundersen, B. G. Novitch, Functional neuromuscular junctions formed by embryonic stem cell-derived motor neurons. *PLoS One* **7**, e36049 (2012).
14. J. C. Piña-Crespo *et al.*, High-frequency hippocampal oscillations activated by optogenetic stimulation of transplanted human ESC-derived neurons. *J. Neurosci.* **32**, 15837–15842 (2012).
15. M. K. Zachek, P. Takmakov, B. Moody, R. M. Wightman, G. S. McCarty, Simultaneous decoupled detection of dopamine and oxygen using pyrolyzed carbon microarrays and fast-scan cyclic voltammetry. *Anal. Chem.* **81**, 6258–6265 (2009).
16. N. T. Rodeberg, S. G. Sandberg, J. A. Johnson, P. E. M. Phillips, R. M. Wightman, Hitchhiker's guide to voltammetry: Acute and chronic electrodes for in vivo fast-scan cyclic voltammetry. *ACS Chem. Neurosci.* **8**, 221–234 (2017).
17. D. Khodagholy *et al.*, In vivo recordings of brain activity using organic transistors. *Nat. Commun.* **4**, 1575 (2013).
18. C. Cvetkovic, M. H. Rich, R. Raman, H. Kong, R. Bashir, A 3D-printed platform for modular neuromuscular motor units. *Microsyst. Nanoeng.* **3**, 17015 (2017).
19. R. D. Kamm *et al.*, Perspective: The promise of multi-cellular engineered living systems. *APL Bioeng* **2**, 040901 (2018).
20. H. B. Baker, J. P. McQuilling, N. M. P. King, Ethical considerations in tissue engineering research: Case studies in translation. *Methods* **99**, 135–144 (2016).
21. S. M. Willerth, K. J. Arendas, D. I. Gottlieb, S. E. Sakiyama-Elbert, Optimization of fibrin scaffolds for differentiation of murine embryonic stem cells into neural lineage cells. *Biomaterials* **27**, 5990–6003 (2006).
22. A. R. Bento, P. Quelhas, M. J. Oliveira, A. P. Pêgo, I. F. Amaral, Three-dimensional culture of single embryonic stem-derived neural/stem progenitor cells in fibrin hydrogels: Neuronal network formation and matrix remodelling. *J. Tissue Eng. Regen. Med.* **11**, 3494–3507 (2017).
23. A. R. Wufsus *et al.*, Elastic behavior and platelet retraction in low- and high-density fibrin gels. *Biophys. J.* **108**, 173–183 (2015).
24. R. Raman, C. Cvetkovic, R. Bashir, A modular approach to the design, fabrication, and characterization of muscle-powered biological machines. *Nat. Protoc.* **12**, 519–533 (2017).
25. K. A. Jansen, P. Atherton, C. Ballestrem, Mechanotransduction at the cell-matrix interface. *Semin. Cell Dev. Biol.* **71**, 75–83 (2017).
26. A. P. Van Winkle, I. D. Gates, M. S. Kallos, Mass transfer limitations in embryoid bodies during human embryonic stem cell differentiation. *Cells Tissues Organs* **196**, 34–47 (2012).
27. R. C. Gonzalez, R. E. Woods, S. L. Eddins, *Digital Image Processing Using MATLAB* (Prentiss Hall, 2003).
28. T. H. Nguyen, M. E. Kandel, M. Rubessa, M. B. Wheeler, G. Popescu, Gradient light interference microscopy for 3D imaging of unlabeled specimens. *Nat. Commun.* **8**, 210 (2017).
29. P. Tanapat, Neuronal cell markers. *Mater. Methods* **3**, 196 (2013).
30. A. Czechanski *et al.*, Derivation and characterization of mouse embryonic stem cells from permissive and nonpermissive strains. *Nat. Protoc.* **9**, 559–574 (2014).
31. T. Kodama *et al.*, Neuronal classification and marker gene identification via single-cell expression profiling of brainstem vestibular neurons subserving cerebellar learning. *J. Neurosci.* **32**, 7819–7831 (2012).
32. N. Matsushita *et al.*, Dynamics of tyrosine hydroxylase promoter activity during midbrain dopaminergic neuron development. *J. Neurochem.* **82**, 295–304 (2002).
33. E. Weihe, C. Depboylu, B. Schütz, M. K.-H. Schäfer, L. E. Eiden, Three types of tyrosine hydroxylase-positive CNS neurons distinguished by dopa decarboxylase and VMAT2 co-expression. *Cell. Mol. Neurobiol.* **26**, 659–678 (2006).
34. E. V. Jones, D. S. Bouvier, Astrocyte-secreted matricellular proteins in CNS remodelling during development and disease. *Neural Plast.* **2014**, 321209 (2014).
35. C. S. Barros, S. J. Franco, U. Müller, Extracellular matrix: Functions in the nervous system. *Cold Spring Harb. Perspect. Biol.* **3**, a005108 (2011).
36. K. S. Midwood, M. Chiquet, R. P. Tucker, G. Orend, Tenascin-C at a glance. *J. Cell Sci.* **129**, 4321–4327 (2016).
37. J. Chen *et al.*, The extracellular matrix glycoprotein tenascin-C is beneficial for spinal cord regeneration. *Mol. Ther.* **18**, 1769–1777 (2010).
38. M. M. Daadi *et al.*, Optogenetic stimulation of neural grafts enhances neurotransmission and downregulates the inflammatory response in experimental stroke model. *Cell Transplant.* **25**, 1371–1380 (2016).
39. P. Soundararajan, G. B. Miles, L. L. Rubin, R. M. Brownstone, V. F. Rafuse, Motoneurons derived from embryonic stem cells express transcription factors and develop phenotypes characteristic of medial motor column neurons. *J. Neurosci.* **26**, 3256–3268 (2006).
40. T. J. Heikkilä *et al.*, Human embryonic stem cell-derived neuronal cells form spontaneously active neuronal networks in vitro. *Exp. Neurol.* **218**, 109–116 (2009).
41. M. D. Neely *et al.*, DMH1, a highly selective small molecule BMP inhibitor promotes neurogenesis of hiPSCs: Comparison of PAX6 and SOX1 expression during neural induction. *ACS Chem. Neurosci.* **3**, 482–491 (2012).
42. S. M. Chambers *et al.*, Combined small-molecule inhibition accelerates developmental timing and converts human pluripotent stem cells into nociceptors. *Nat. Biotechnol.* **30**, 715–720 (2012).
43. W. Li *et al.*, Rapid induction and long-term self-renewal of primitive neural precursors from human embryonic stem cells by small molecule inhibitors. *Proc. Natl. Acad. Sci. U.S.A.* **108**, 8299–8304 (2011).
44. J. C. Butts *et al.*, Differentiation of V2a interneurons from human pluripotent stem cells. *Proc. Natl. Acad. Sci. U.S.A.* **114**, 4969–4974 (2017).
45. C.-Y. Wu, D. Whye, R. W. Mason, W. Wang, Efficient differentiation of mouse embryonic stem cells into motor neurons. *J. Vis. Exp.* **2012**, e3813 (2012).

Pagan-Diaz et al.

www.manaraa.com